

ON PROBING THE PROPERTIES OF QSOS THROUGH THEIR PROXIMITY EFFECTS ON THE INTERGALACTIC MEDIUM

YOUJUN LU¹ & QINGJUAN YU²

¹ National Astronomical Observatories, Chinese Academy of Sciences, Beijing, 100012, China; luyj@nao.cas.cn

² Kavli Institute for Astronomy and Astrophysics, Peking University, Beijing, 100891, China; yuqj@pku.edu.cn

Draft version January 20, 2013

ABSTRACT

The proximity effect (PE) of QSOS is believed to be useful in constraining the QSO lifetime. Observations on the PE so far, however, give apparently contradictory results – some are consistent with a long QSO lifetime (\gtrsim a few 10^7 yr), but others appear to be only consistent with a short QSO lifetime $\lesssim 10^6$ yr. In this paper, we show that this apparent contradiction may be solved by simultaneously taking into account both the effect due to the density enhancement in the QSO near zones and that due to the obscuration of the tori associated with the QSOS, using a large number of Monte-Carlo generated synthetic Ly α forest spectra. We demonstrate that the QSO properties and environment can be constrained simultaneously by the transverse PE and the line of sight PE of bright type 1 QSOS together. The current available measurements on the PEs of type 1 QSOS suggest that (1) the density is significantly enhanced in the vicinity of the QSOS; (2) the QSO lifetime is consistent with being as large as a few 10^7 yr and a substantially shorter lifetime (e.g., $\lesssim 10^6$ yr) is not required; and (3) the half opening angle of the tori associated with QSOS is $\sim 60^\circ$, consistent with some other independent estimates. Our simulations also show that the TPE of type 2 QSOS can be significantly different from that of type 1 QSOS, which may be useful to put further constraints on the QSO properties and the QSO environment.

Subject headings: intergalactic medium–quasars: absorption lines–quasars: general–black hole physics

1. INTRODUCTION

The enormous UV radiation from a QSO can significantly alter the ionization state of its surrounding intergalactic medium (IGM). The Ly α absorption clouds near the QSO are more ionized than average, and the optical depth of Ly α photons due to the absorbers was expected to decrease as the absorption redshift approaches that of the QSO, which is named as the “proximity effect” (PE) (Carswell 1987; Bajtlik et al. 1988). The significance of the PE of a QSO is mainly determined by the following factors: (1) the strength of the metagalactic UV ionizing background (UVB); (2) the intrinsic properties of the QSO, including its luminosity, its age (or its detailed luminosity evolution), and the anisotropic feature in its UV radiation; and (3) the overdense environment of the IGM surrounding the QSO. Therefore, the PE is useful not only to measure the UVB (e.g., Bajtlik et al. 1988), but also to constrain the lifetime/luminosity evolution of QSOS and the density enhancement in its near zones (e.g., Jakobsen et al. 2003; Croft 2004; Schirber et al. 2004; Adelberger 2004; Rollinde et al. 2005; Guimarães et al. 2007; Kirkman & Tytler 2008; Gonçalves et al. 2008).

The PE along the line of sight to a QSO (LOSPE) has been clearly detected through the high-resolution Ly α absorption spectra of a combined QSO sample or some individual QSOS, which is widely used to estimate the strength of the UVB (e.g., Scott et al. 2000; Dall’Aglio et al. 2008) and also the density enhancement of the IGM surrounding the QSO (e.g., Rollinde et al. 2005; Guimarães et al. 2007). For example, Dall’Aglio et al. (2008) and Faucher-Giguère et al. (2008b) find that the UVB measured from the LOSPE (after including the effect of the overdense environment of

QSOS) is consistent with those estimates obtained from other methods. The LOSPE is affected directly by the observed QSO luminosity, but almost irrelevant to the QSO’s past luminosity evolution (including luminosity variation) and the age of its nuclear activity. In principle, the PE may be also affected by fluctuations in the QSO luminosity on short timescales $\lesssim 2 \times 10^4$ yr, over which the perturbed ionization state of the highly ionized IGM can get back to the photoionization equilibrium. However, the QSO variability studies give the average lifetime of an individual episode of QSO activity $\gtrsim 10^4$ yr (e.g., Martini & Schneider 2003; Martini 2004).

The PE in the region other than along the line of sight to the QSO (i.e., the transverse PE or TPE) can be measured through the spectra of background QSOS (bgQSOS) or other bright UV sources whose light passed through the highly ionized region surrounding the foreground QSOS (fgQSOS). Unlike the LOSPE, the TPE should be sensitive to the age of the fgQSO, as a positive detection of this effect requires that the light travel time from the fgQSO to the line of sight (LOS) to the bgQSO is smaller than the age of the fgQSO. Hence, the TPE has long been thought to be helpful in constraining the QSO lifetime (e.g., Bajtlik et al. 1988; Croft 2004; Schirber et al. 2004; Adelberger 2004; Kirkman & Tytler 2008). However, so far the results from observations on the significance of the TPE appear ambiguous. For example, many authors tried to search for the reduction in the optical depth or the number of HI Ly α forest lines caused by the TPE through QSO pairs with small transverse separation (typically \lesssim a few Mpc), but they found no evidence of this reduction and suggested that the QSO lifetime $\lesssim 10^6$ yr (e.g., Fernández-Soto et al. 1995; Crofts & Fang 1998; Croft 2004; Schirber et al.

2004; Kirkman & Tytler 2008). However, several authors have reported the detections of the TPE through the observations on the He II, rather than H I, Ly α forest or metal absorption lines (e.g., Jakobsen et al. 2003; Worseck & Wisotzki 2006; Worseck et al. 2007; Gonçalves et al. 2008). Those detections suggest that the QSO lifetime should be $\gtrsim 10^7$ yr. Currently it is still unclear whether that apparent contradiction is due to some selection effects in observations or the complications introduced by other factors, such as, the density enhancement in the QSO near zones or the anisotropic radiation from QSOs.

In this paper, we study the LOSPE and the TPE of QSOs, with taking into account the density enhancement in the QSO proximity region, their anisotropic UV radiation, and their lifetime; and the purpose is not only to solve the apparent contradiction among the observational constraints on the QSO lifetime from current TPE observations, but also to demonstrate that the LOSPE and the TPE combine to put constraints on both the QSO lifetime and the opening angle of torus associated with QSOs simultaneously. The paper is organized as follows. In Section 2, we illustrate the geometry of the proximity region of a QSO in the observer's rest frame that can be affected by UV photons emitted from the QSO. Accounting the PE of (fg)QSOs, we use a Monte-Carlo method to generate a large number of Ly α forest spectra of fgQSOs and bgQSOs as described in Section 3, based on some statistical distributions of the HI column density, the Doppler factor of Ly α absorption lines, and the redshift distribution of the number density of these lines (see Dall'Aglio et al. 2008, 2009). With these synthetic Ly α forest spectra, we illustrate both the optical depth decrease due to the LOSPE and the TPE of QSOs and then compare them with current observational results on type 1 QSOs in Section 4. Considering that future X-ray observations potentially discover a large number of type 2 QSOs, the TPE of type 2 QSOs is also investigated in Section 4. Our simulation results demonstrate that the density enhancement near the QSOs, the QSO lifetime, and the opening angle of the tori associated with the QSOs can be simultaneously constrained through measurements on both the LOSPE and the TPE. Discussions and conclusions are given in Section 5.

In the paper, We adopt the Hubble constant $H_0 = 71 \text{ km s}^{-1}$ and the cosmological parameters (Ω_m, Ω_Λ) = (0.27, 0.73) (Komatsu et al. 2009).

2. GEOMETRY OF THE PROXIMITY REGION OF A QSO

In this section, we illustrate how the geometry of the proximity region of a fgQSO in the distant observer's frame is affected by the age of the QSO and the anisotropic feature of its radiation. In general, we describe the region near a fgQSO by the physical distance of a point from the QSO R and its polar angle θ measured from the observer's LOS (i.e., OC in Figure 1).

From Ly α forest spectra, the distant observer deduces the proximity region which can be affected by the fgQSO radiation through the light passing by the region. Considering the finite speed of the light, the combination of the light traveling time from the affected region to the observer and the time of the fgQSO light traveling from its location to its affected region should not be longer than the light traveling time from the fgQSO to the observer

by the QSO age. That is, in the distant observer's rest frame, photons emitted from the QSO can reach a physical distance of at most $R_*(\theta_*) = |\text{OA}|$ from the QSO as shown in Figure 1, and $R_*(1 - \cos \theta_*) = c\tau_Q$, where θ_* is the angle of OA from the observer's LOS OC, τ_Q is the QSO age, and c is the speed of light. The $R_*(\theta_*)$ gives the apparent time-delay envelope within which the ionization state of (hydrogen) atoms can be possibly affected by UV radiation from the QSO.

Considering a bgQSO of which the LOS to the observer is separated from the fgQSO by a transverse proper distance of R_\perp , the intersection point of the bgQSO LOS with the time-delay envelope (point A in Figure 1) is given by $\theta_* = 2 \arctan(c\tau_Q/R_\perp)$. The Ly α forest in the spectrum of the bgQSO may be then affected by the fgQSO at observational wavelength $\lambda \leq 1216\text{\AA}(1+z_A)$, where z_A is the redshift of the interaction point A. We have $z_A \simeq z_{\text{fg}} - (1+z_{\text{fg}})E(z_{\text{fg}})R_{\parallel,A}/c$, where z_{fg} is the redshift of the fgQSO, $R_{\parallel,A} = \frac{\cos \theta_*}{1 - \cos \theta_*} c\tau_Q$ is the physical distance from A to B shown in Figure 1, point B is located on the LOS to the bgQSO and has the same distance/redshift to the observer as the fgQSO, and $E(z) = H_0 \sqrt{\Omega_m(1+z)^3 + \Omega_\Lambda}$. The photoionization enhancement at a particular point on the LOS to the bgQSO due to the fgQSO can be characterized by the ratio of $\omega \equiv \Gamma_{\text{QSO}}/\Gamma_{\text{UVB}}$, where Γ_{QSO} is the photoionization rate due to the QSO UV radiation and Γ_{UVB} is the photoionization rate due to the cosmic UVB. The latest constraints on the cosmic UVB show that Γ_{UVB} is roughly a constant over redshift from 2 to 4 (e.g., $\sim 0.5 \times 10^{-12} \text{ s}^{-1}$ in Faucher-Giguère et al. 2008a, $\sim 1 - 1.3 \times 10^{-12} \text{ s}^{-1}$ in Bolton et al. 2005, see also Haardt & Madau 1996; Rauch et al. 1997; McDonald & Miralda-Escudé 2001; Meiksin & White 2004; Tytler et al. 2004; Kirkman et al. 2005). In this paper, we choose $\Gamma_{\text{UVB}} \simeq 10^{-12} \text{ s}^{-1}$. The Γ_{QSO} at a distance R from the fgQSO is $\int_{\nu_0}^{\infty} \frac{L_{\text{QSO},\nu}(t)}{4\pi R^2} \frac{\sigma_{\text{HI}}(\nu)}{h\nu} d\nu$, where $L_{\text{QSO},\nu}(t)$ is the luminosity of the QSO per unit frequency at its intrinsic frequency ν emitted at time $t = \tau_Q - R(1 - \cos \theta)/c$ since its nuclear activity is triggered, ν_0 is the Lyman limit frequency, $\sigma_{\text{HI}}(\nu) \propto \nu^{-3}$ is the HI photoionization cross-section (Osterbrock 1989), and R can be approximated as the corresponding luminosity distance as long as it is small enough. In this paper, we assume $L_{\text{QSO},\nu} \propto (\nu/\nu_0)^{-0.5}$. Due to the time delay, we have $\Gamma_{\text{QSO}} = 0$ and $\omega = 0$ at those points with $R > R_*(\theta)$.

In the AGN unification model (e.g., Urry & Padovani 1995), however, the UV radiation from a QSO can be highly anisotropic depending on whether the torus associated with the QSO blocks its radiation along the LOS to the observer, and this geometrical effect results in the observational differences between type 1 and type 2 QSOs. The anisotropic radiation of QSOs leads to different ionization states of its surrounding IGM in different directions and thus we may have different observational PEs for type 1 and type 2 QSOs as follows.

- For a type 1 QSO, the UV radiation may be blocked in the transverse direction and the ionization state of the IGM in that direction may be not affected by the UV photons from the QSO. We denote the half opening angle of the dusty torus associated

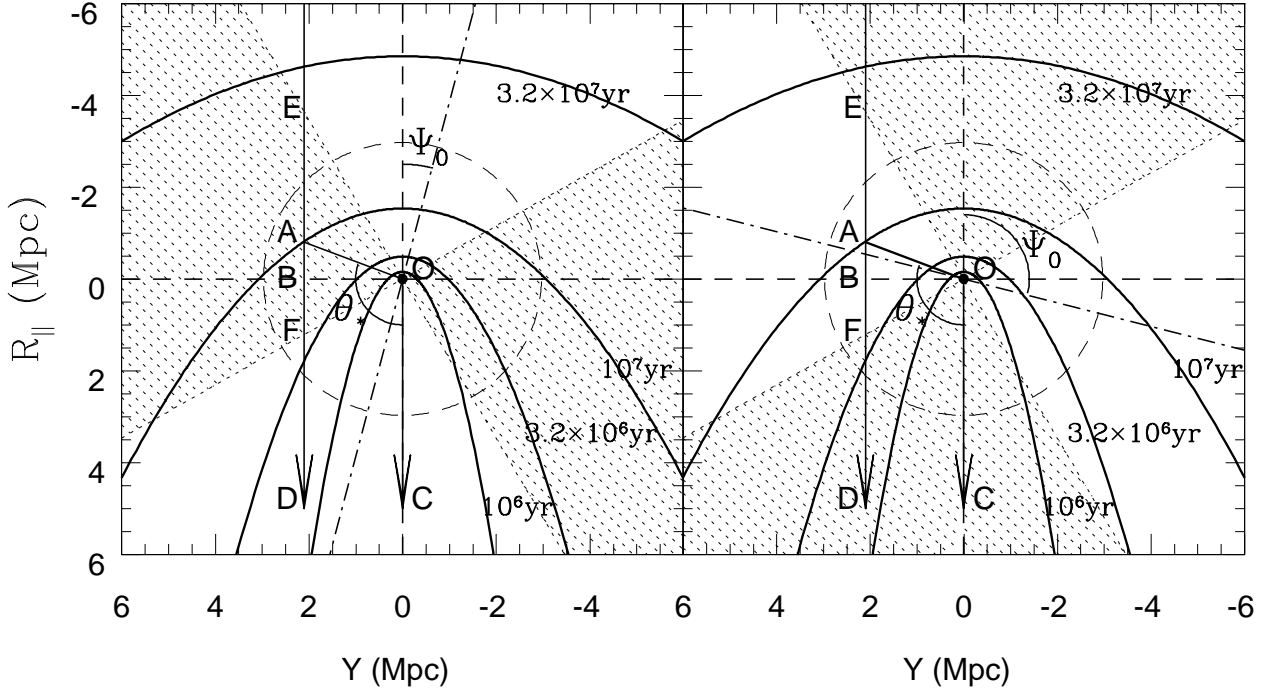


FIG. 1.— Schematic diagram for the proximity region of a fgQSO that may be affected by the UV photons emitted from it. The fgQSO is at point O, and the distant observer is located in the direction OC. The ED is the direction from a background bright UV source or QSO to the observer. The left and right panels illustrate the cases for a type 1 fgQSO and a type 2 fgQSO, respectively. The intrinsic QSO UV radiation is assumed to be isotropic, but it may be shielded in some directions by a dusty torus as shown by the shaded area in both panels. The half opening angle of the torus is $\Theta_0 = 45^\circ$, and the offset of the torus axis (the dot-dashed lines) from the direction OC is $\Psi_0 = 15^\circ$ in the left panel and 105° in the right panel, respectively. The shaded region is rotationally symmetric around the torus axis. For illustration purpose, the LOS to the bgQSO is assumed to be specifically on the plane of the torus axis and the LOS to the fgQSO (see Appendix for discussion on more general cases); and it has a physical distance of $R_\perp = |OB|$ from the fgQSO and interacts with the shaded region at points E and F. The thick solid curves represent the envelope surfaces of the proximity regions that can be affected by the fgQSO radiation for the QSO age of 3.2×10^7 yr, 10^7 yr, 3.2×10^6 yr, and 10^6 yr (from top to bottom), respectively. These surfaces are rotationally symmetric around the LOS to the fgQSO. The dashed circle represents the surface on which the photoionization rate enhancement due to the central QSO is $\omega \equiv \Gamma_{\text{QSO}}/\Gamma_{\text{UVB}} = 1$. Here the QSO is set to be at redshift $z_{\text{fg}} = 2$ with a Lyman limit luminosity of $10^{30.5} \text{ erg s}^{-1} \text{ Hz}^{-1}$, and the photoionization rate due to the UVB $\Gamma_{\text{UVB}} = 10^{-12} \text{ s}^{-1}$.

with the fgQSO by Θ_0 ($0^\circ \leq \Theta_0 \leq 90^\circ$) and the torus axis offset from the LOS by an angle of Ψ_0 ($0^\circ \leq \Psi_0 < 180^\circ$; see the left panel of Figure 1). The intersections of the bgQSO LOS with the light cone confined by the torus associated with the fgQSO are E and F. Given a transverse distance R_\perp , the proper distances from E to B and F to B are given by the two solutions ($R_{\parallel,E}$, $R_{\parallel,F}$) of the equations governing the light cone and the cylinder with a radius of R_\perp (see details in Appendix), and correspondingly the redshifts of E and F are given by $z_E \simeq z_{\text{fg}} - (1 + z_{\text{fg}})E(z_{\text{fg}})R_{\parallel,E}/c$ and $z_F \simeq z_{\text{fg}} - (1 + z_{\text{fg}})E(z_{\text{fg}})R_{\parallel,F}/c$, respectively. Therefore, the UV photons from the fgQSO can only affect the spectrum of the bgQSO in the wavelength ranges of $1216\text{\AA} \min(1 + z_E, 1 + z_A) \leq \lambda \leq 1216\text{\AA}(1 + z_A)$ and $\lambda \leq 1216\text{\AA} \min(1 + z_A, 1 + z_F)$ as $z_E > z_F$ (see the left panel of Figure 1). Outside of these wavelength ranges, $\omega = 0$.

- For a type 2 QSO, the UV radiation is blocked from the view of a distant observer by a dusty torus. This QSO cannot be seen in the optical-UV band but is detectable in the hard X-ray. However, the UV radiation from a type 2 QSO may significantly alter the ionization state of the IGM in the transverse direction of its proximity region (see the right panel in Figure 1). For a type 2 QSO, the UV photons can affect the Ly α forest spectrum of a bgQSO

in the wavelength range of $1216\text{\AA} \min(1 + z_E, 1 + z_A) \leq \lambda \leq 1216\text{\AA} \min(1 + z_A, 1 + z_F)$ (see the right panel of Figure 1). For those cases without solutions to the two equations, the spectrum of the bgQSO is not affected by the PE with $\omega = 0$.

We note here that the TPE of type 2 fgQSOs could be the same as that of type 1 fgQSOs if the obscuration, which leads to the classification of type 1 and type 2 QSOs, is due to isotropically distributed clumpy absorbers, rather than the uniform torus-like structure.

3. MONTE-CARLO SIMULATIONS OF SYNTHETIC SPECTRA OF LY α FORESTS NEAR A FGQSO

In principle, both the LOSPE and TPE can be well understood by detailed 3D numerical simulations that can successfully reproduce the Ly α forest at any redshift (e.g., Croft 2004; Schirber et al. 2004; Faucher-Giguère et al. 2008b). Those simulations with detailed radiative transfer may be able to accommodate all the statistical and systematic effects and the density enhancement in the vicinity of QSOs, but they are very time consuming and dependent on the assumptions of the QSO host dark matter halos. In this paper, we alternatively adopt a Monte Carlo method, proposed by Worseck & Wisotzki (2006, see also Dall’Aglio et al. 2008, 2009), to generate Ly α forest spectra for a large number of LOSs. This Monte-Carlo method has been demonstrated to be able to reproduce the Ly α forest

spectra of QSOs similar to observed ones and be useful in measuring the UVB through the QSO proximity effect (Dall’Aglio et al. 2008). With detailed statistical consideration on different factors that may affect the proximity effect of the fgQSOs, including the QSO age, the anisotropic UV radiation and the density enhancement, etc. (as discussed in Section 2), we simulate both the LOSPE and TPE for a large number of fgQSOs.

The procedure adopted to generate the mock QSO Ly α forest spectra is based on the observations that each Ly α absorption line with Voigt profile can be described by the HI column density N_{HI} and the Doppler parameter b of its corresponding absorption gas and that the comoving number density of the absorption lines per unit z , N_{HI} , and b , denoted by $n(z, N_{\text{HI}}, b)$, can be well described by the following three distributions:

1. the redshift distribution, approximated by a power-law form with $n \propto (1+z)^\gamma$, where $\gamma = 2.13$ (Kim et al. 2001; Schaye et al. 2003, see also Faucher-Giguère et al. 2008c);
2. the HI column density distribution with $n \propto N_{\text{HI}}^{-\beta}$, where the power $\beta \simeq 1.5$ (Kim et al. 2001);
3. the Doppler parameter distribution with $n \propto b^{-5} \exp[-b_\sigma^4/b^4]$ where $b_\sigma \simeq 24 \text{ km s}^{-1}$ (Kim et al. 2001).

The column densities of the simulated absorbers are limited to be within the range $10^{12} \text{ cm}^{-2} < N_{\text{HI}} < 10^{18} \text{ cm}^{-2}$ and the Doppler parameters within $10 \text{ km s}^{-1} < b < 100 \text{ km s}^{-1}$. Those three distributions are assumed to be independent one another. For the purpose of this paper, we populate absorbers in each line of sight according to the above distributions and generate mock samples of the Ly α forest spectra. Gaussian noise is added to the simulated Ly α forest spectra and the spectral resolution is also considered in order to match the signal-to-noise level of those observed samples discussed in Section 4. For simplicity, the emission lines are not added to the spectra of mock QSOs. Note that the adopted Monte-Carlo method naturally includes the Poisson variance of the number of absorption lines in the near zone of fgQSOs (e.g., Dall’Aglio et al. 2008).

In the QSO near zones, the mass density may be significantly enhanced relative to the cosmic average density, i.e., $\langle \Delta(R) \rangle \equiv \langle \rho(R) \rangle / \bar{\rho} > 1$, where $\langle \Delta(R) \rangle$ and $\langle \rho(R) \rangle$ is the mass overdensity and the mass density at a distance R from central QSOs averaged over a large sample of QSOs with similar properties, respectively, and $\bar{\rho}$ is the cosmic average density. A simple photoionization equilibrium model can give the neutral hydrogen density of an absorber $n_{\text{HI}} \propto \delta^{2-0.7\eta}$, where δ is the mass overdensity of the absorber δ and $\eta \sim 0.62$ is the index of the power-law temperature-density relation for the low-temperature IGM (e.g., Faucher-Giguère et al. 2008b; Schaye 2001; Hui & Gnedin 1997). Assuming that the column density distribution of Ly α absorbers in the QSO near zones (with mean density enhancement factor $\langle \Delta(R) \rangle$) also follows a power law $\propto N_{\text{HI}}^{-\beta}$ with the same slope β as that for the cosmic average (item 2 listed above), the column density of each absorber generated from the above distribution (item 2) should then be replaced by $N_{\text{HI}} \langle \Delta(R) \rangle^{2-0.7\eta} / (1+\omega)$, considering of

both the effects of the enhanced density and UV ionizing flux in QSO near zones (cf., see Equation 30 in Faucher-Giguère et al. 2008b). Note that the effect of that replacement is equivalent to the effect of increasing the number of absorbers proportionally.

As illustrated in Figure 1, different choices of the fgQSO age, the half opening angle Θ_0 , and the offset angle Ψ_0 of the torus associated with the fgQSO will affect the proximity region that the fgQSO can illuminate. In our simulations, we set seven different values for the lifetime of QSOs τ_t , and the QSO age τ_Q is either fixed or randomly chosen over the range $(0, \tau_t)$. We choose six sets of values for the opening angle of the torus, i.e., $\Theta_0 = 0^\circ, 30^\circ, 45^\circ, 60^\circ, 72^\circ$, and 89° . The $\Theta_0 = 0^\circ$ corresponds to the cases of no ionization PE from the central QSOs, and the $\Theta_0 = 89^\circ$ corresponds closely to no obscuration to the UV radiation from the fgQSOs. The other specific values of Θ_0 , i.e., $30^\circ, 45^\circ, 60^\circ$, and 72° , are chosen as their corresponding abundance ratios of type 2 to type 1 QSOs (6.5, 2.4, 1, and 0.4, respectively) are roughly in the range estimated by observations (e.g., Treister & Urry 2006; Gilli et al. 2007; Treister et al. 2010). We also randomly choose Ψ_0 within the range from Θ_0 to $180^\circ - \Theta_0$ for type 2 QSOs, and other range for type 1 QSOs.

According to the above settings, we first simulate the Ly α forest spectra of QSOs affected by its own UV radiation to account for the LOSPE. In order to compare with the observational results on the LOSPE (and the TPE later) by Kirkman & Tytler (2008) (hereafter KT08) obtained from a sample of 130 QSO pairs, the observational redshift of the fgQSOs and its luminosities at the Lyman limit frequency in our simulation are set to be $z_{\text{fg}} = 2$ and $L_{\nu_0} = 5 \times 10^{30} \text{ erg s}^{-1} \text{ Hz}^{-1}$, which are roughly the mean redshift and luminosity of the sample in KT08. Note that most of the QSOs in KT08 sample are in the redshift range $z \sim 1.8 - 2.6$, and the redshift dependence of the optical depth has been corrected in KT08. As the actual halos hosting these fgQSOs and the overdensity distribution surrounding them are not well known, we only consider the average effects of the sample in this paper, not going to the detailed redshift and luminosity distributions of QSOs as shown in the KT08 sample. We first create 100 realizations of 130 independent synthetic spectra to check whether the sample variance could be significant in the interpretation of the observational results. And then we also create larger mock samples with 500 independent synthetic Ly α forest spectra to check whether the QSO properties can be extracted effectively from a sample with 500 spectra or more. Similar to KT08, the amount of absorption in each spectrum of the mock samples is quantified by $DA \equiv 1 - F/C$, where F is the flux and C is the continuum level, and a uniform flux decrement due to the metal absorption $DA_{\text{metal}} = 0.025$ is also added to each spectrum at wavelength higher than the Ly α emission line. We also simulate the Ly α forest spectra of bgQSOs, which are affected by the UV radiation from fgQSOs, to account for the TPE. The transverse distances of fgQSOs from the LOS to their bgQSOs R_\perp are randomly chosen from 0.1 Mpc to 3 Mpc, within the range of the observational sample in KT08. We also create 500 independent synthetic spectra for each set of parameters ($\tau_{\text{age}}, \Theta_0$) for both type 1 and type 2 fgQSOs,

respectively. For each mock sample, we then obtain the average flux decrement $\langle DA \rangle$ of the 500 spectra. Comparison of the simulated LOSPE and TPE with the observations may thus put some constraints on the intrinsic properties of QSOs.

Similarly, we create 500, if not otherwise specified, independent synthetic spectra of a QSO/bgQSO, which are affected by either its own UV radiation or the UV radiation from a fgQSO at $z_{\text{fg}} = 4$ with a mean Lyman limit luminosity of $L_{\nu_0} = 8 \times 10^{31} \text{ erg s}^{-1} \text{ Hz}^{-1}$, for each set of parameters (η_t , Θ_0). The LOSPE obtained from the set of synthetic Ly α forest spectra can be used to compare with that obtained by Guimarães et al. (2007) for a sample of QSOs with similar redshift and mean Lyman limit luminosity. Similar to Guimarães et al. (2007), the absorption here is quantified by the median of the optical depths $\tau \equiv -\ln(F/C)$ of all the LOSs. With some constraints obtained from the LOSPE observations by Guimarães et al. (2007), we also obtain the expected TPE of type 1 and type 2 fgQSOs from the mock samples.

4. SIMULATION RESULTS

We illustrate the simulation results on both the LOSPE and TPE for both the samples with relatively low luminosities at low redshift ($z \sim 2$ and $L_{\nu_0} \sim 5 \times 10^{30} \text{ erg s}^{-1} \text{ Hz}^{-1}$; Section 4.1) and the samples with high luminosities at high redshift ($z \sim 4$ and $L_{\nu_0} \sim 8 \times 10^{31} \text{ erg s}^{-1} \text{ Hz}^{-1}$; Section 4.2). In order to compare with those observations by KT08 and Guimarães et al. (2007), the spectra are averaged over resolution of 1 Å and 0.3 Å, and the signal to noise ratio are set to be 11.2 and 25 for the low-luminosity and high-luminosity samples similar to those in KT08 and Guimarães et al. (2007), respectively. Along with the detailed presentation on how the detected PEs can be affected by the QSO lifetime, the geometric structure of the torus, and the QSO environment below, the effect of different QSO luminosities is also revealed.

4.1. Low-luminosity samples at $z \sim 2$

4.1.1. The LOSPE of type 1 fgQSOs

Figure 2 shows the average absorption near QSOs/fgQSOs along their LOS with the origin corresponding to their redshift. The histogram with error bars shows the DA measured by KT08. The color lines and symbols in panels (a) and (b) show the results obtained from 100 realizations of a mock sample with 130 synthetic Ly α forest spectra and the results from a mock sample with 500 synthetic spectra, respectively. The value plotted for each bin is the mean value of DA from the Ly α forest spectra, and the error bar is taken to be standard deviation of the 100 realizations in panel (a) and the standard error of the mean in panel (b), respectively. The color lines and symbols show the expected DA estimated by assuming the following several cases: (1) on average the density in the QSO near zones is not enhanced (blue line and points), i.e., $\langle \Delta(R) \rangle = 1$; or (2) there is no UV radiation from the central QSOs and on average the density near the QSO is not enhanced, i.e., $\omega = 0$ and $\langle \Delta(R) \rangle = 1$ (green line and points); or (3) there is a density enhancement near the QSO described by $\langle \Delta(R) \rangle \sim 1 + C_0(R/C_R)^{-p} \exp[-(R/C_R)^q]$

with $C_0 = 2.2$, $C_R = 3.0 \text{ Mpc}$, $p = 0.7$, and $q = 2.0$ (red line and points)¹. As shown in panels (a) and (b), the histogram is systematically and substantially higher than the blue line but consistent with the green line (no LOSPE), which suggests that the sample variance is highly unlikely to be responsible for the excess of absorption in the QSO near zone and the density in the QSO near zones is enhanced. Indeed, the expected DA can be consistent with the observations if the density is enhanced in the QSO near zone (as shown by the red line and points in panels a and b). Note also that the error to the mean of DA for a sample of 500 spectra is sufficiently small, which suggests that the physical properties of QSOs can be extracted from the PE for samples with 500 spectra or more.

The PE analysis is sensitive to the accuracy in the systemic redshift estimation of each QSO/fgQSO being studied if the size of its proximity region is smaller than or comparable to the scale corresponding to the systemic redshift error. However, the systemic redshift estimated from the UV emission lines of a QSO is generally systematically smaller than the systemic redshift of its host galaxy by more than a few hundred kilometer per second. Richards et al. (2002) find that CIV gives a redshift smaller than Mg II by 824 kms^{-1} with a scatter of 511 kms^{-1} from a subset of SDSS QSO spectra. Nestor et al. (2008) find that the [OIII], which should better represent the systemic redshift, gives a systemic redshift larger than Mg II by 102 kms^{-1} . According to these results, the errors in the systemic redshift estimates of QSOs can be divided into two parts, i.e., the mean systematic offset and the scatter around the mean offset, which are denoted as the “systematic error” and the “random error” below, respectively. According to Richards et al. (2002) and Nestor et al. (2008), we adopt a systematic error of 926 kms^{-1} in the estimates of the fgQSO systemic redshifts and a random error with dispersion 511 kms^{-1} (as the redshift of the majority of the QSOs in KT08 is estimated by CIV), unless otherwise specified. Note that the systematic error adopted in KT08 is smaller, $\sim 753 \text{ kms}^{-1}$, and the dispersion of the random errors is 676 kms^{-1} , and we also try those errors in our simulations below (i.e., in Figure 5, where the systemic redshift of each mock QSO is set to be a value of $z_{\text{fg}} = 2$ plus a Gaussian distributed random error). In order to compare with the observational results from KT08, an additional correction in the systematic error of $\langle \delta z_{\text{offset}} \rangle = 173 \text{ kms}^{-1}$ needs to be taken into account, i.e., the systemic redshift of each QSO host in the mock samples is set to $z_{\text{fg}} + \delta z_{\text{offset}}$, where z_{fg} is set to 2 and the random error in δz_{offset} is also assumed to be Gaussian distributed (e.g., in Figures 2, 3d, 4, 6, 7 below). For comparison, a zero error of δz_{offset} is assumed

¹ Note that this assumed form of $\langle \Delta(R) \rangle$ follows the tendency of approaching 1 at sufficiently distant regions and increasing with the decreased R . Here $\langle \Delta(R) \rangle$ can be taken as the effective density enhancement factor but not the exact physical overdensity of each absorber at R . The physical overdensity of an absorber at R is $\delta \propto \langle \Delta(R) \rangle$. The detailed values used for the involved parameters come empirically from the comparison of our simulation results with the observations below. While this should be sufficient for the purpose of this paper, those constraints may be improved by future high-resolution spectra of QSOs and the PEs to be revealed and the comparison with cosmological simulations of PEs with including detailed 3D radiative transfer processes.

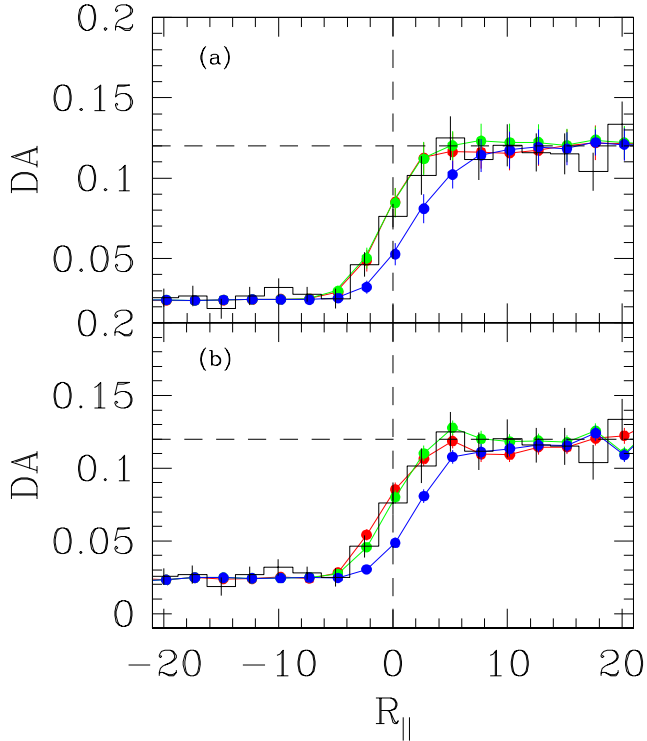


FIG. 2.— The line of sight proximity effect. The histogram in panel a (or b) shows the measured flux decrement DA at a proper distance R_{\parallel} along the LOS from the central QSO, averaged over an observational sample of 130 QSOs with redshift ~ 2 and Lyman limit luminosity $L_{\nu_0} \sim 5 \times 10^{30} \text{ erg s}^{-1} \text{ Hz}^{-1}$ (adopted from KT08). The color lines and points in panel (a) represent the mean DA obtained from 100 realizations of a mock sample with 130 synthetic Ly α forest spectra, where the error bar for each bin is the standard deviation of the sample, while in panel (b) they represent that obtained from mock samples with 500 synthetic Ly α forest spectra, where the error bar is the standard error on the mean. The blue line and solid circles show the simulated DA due to the PE of the central QSOs if the average density in the QSO near zones is similar to the cosmic average; the green line and solid circles show the simulated DA if there is no proximity effect due to the UV radiation from the central QSO and no density enhancement in the QSO near zones; and the red line and solid circles show the simulated DA if the density is enhanced in the QSO near zones effectively by a factor of $\langle \Delta(R) \rangle$ (see details in Section 4.1.1). All the circle points are centered on the same bins of R_{\parallel} as the observational data but have been slightly offset to the right for graphical clarity.

in Figure 3a-c below. Generally, the larger the systematic error in the systemic redshift estimates, the less the enhancement of the density in the fgQSO near zones that is required to reproduce the observed LOSPE (see Figure 2).

4.1.2. The TPE of type 1 fgQSOs

Assuming that the effective density enhancement in the near zones of the fgQSOs is the same as the one required to reproduce the observations on the LOSPE by KT08², we generate mock samples with 500 synthetic Ly α forest spectra and obtain the TPE effect from these samples. Figure 3 shows the expected TPE obtained from the mock samples with different settings of the QSO age τ_Q , the opening angle of the torus Θ_0 , and the error in the estimation of the fgQSO systemic redshift. Fig-

² We assume that the density enhancement in the QSO near zone is isotropic. We do not consider an anisotropic distribution of the density enhancement in this paper.

ure 3a shows that for a small QSO age τ_Q , the excess of DA is significant near the fgQSOs because of the significant density enhancement in the immediate vicinity of the fgQSOs. This excess of DA decreases with increasing τ_Q because the significance of the suppression of the absorption by the UV photons from the fgQSOs increases with increasing τ_Q . In principle, the dependence of the TPE on the QSO age τ_Q , as shown in Figure 3a, suggests that the TPE can be used to constrain the QSO lifetime once the density enhancement in the fgQSO near zones is determined by the LOSPE. The differences among large τ_Q cases shown in the panel are small because the time during which photons cross the proximity regions are smaller than or at most comparable to the QSO age in these cases. However, none of the simulated DA (even the one with the shortest τ_Q) in Figure 3a can match the observational results on the TPE obtained by KT08.

Figure 3b shows the dependence of the TPE on the half opening angle Θ_0 of the tori associated with the fgQSOs. For the extreme case of $\Theta_0 = 0^\circ$ (without the PE due to the fgQSO UV radiation), the excess of the DA due to the density enhancement near fgQSOs is the most significant (red line and points). With increasing Θ_0 , the excess of DA becomes less and less significant because the region that can be affected by the UV photons escaping out from the central engine becomes larger as shown by the color lines and points. For $\Theta_0 = 89^\circ$ (almost without obscuration to the fgQSO photons; magenta line and points), the expected excess of DA due to the density enhancement is balanced significantly by the proximity effect due to the fgQSO UV radiation.

Figure 3c shows the dependence of the TPE on the lifetime of fgQSOs, in which the half opening angle of the torus is fixed to $\Theta_0 = 60^\circ$. This value of Θ_0 is roughly in the range determined by observations (e.g., Treister & Urry 2006; Gilli et al. 2007; Treister et al. 2010). In this panel, the value of the QSO age τ_Q is chosen randomly over a range from 0 to the QSO lifetime τ_t , instead of being a constant as labeled for each line in panel (a). Because of the obscuration in the transverse direction to the UV radiation from the fgQSOs, there is significant DA excess even for the case of $\tau_t = 10^{7.7} \text{ yr}$. Compared to the case without obscuration shown in Figure 3a, the dependence of the DA excess on τ_t becomes less obvious if the obscuration to the UV radiation from the fgQSOs is significant.

Note that one characteristic timescale for the luminosity evolution of a QSO is the Salpeter timescale τ_{sp} , which is $\sim 10^{7.7} \text{ yr}$ if the mass-to-energy conversion efficiency of its nuclear activity is ~ 0.1 and the Eddington ratio is 1. If the age of a fgQSO is larger than the Salpeter timescale, the proximity effect may be substantially less significant for regions faraway from the fgQSOs with $R(1 - \cos \theta_*) \gtrsim c\tau_{\text{sp}}$, considering the luminosity evolution of the fgQSOs may be significant.

Figure 3d shows the expected TPE obtained from the mock samples after taking into account the errors in the systemic redshift of the fgQSOs. As in panel (c), the opening angle of the tori associated with the fgQSOs is fixed to 60° and the age of fgQSOs τ_Q is randomly chosen over a range of $(0, \tau_t)$. As seen from the panel, the observations by KT08 can be well repro-

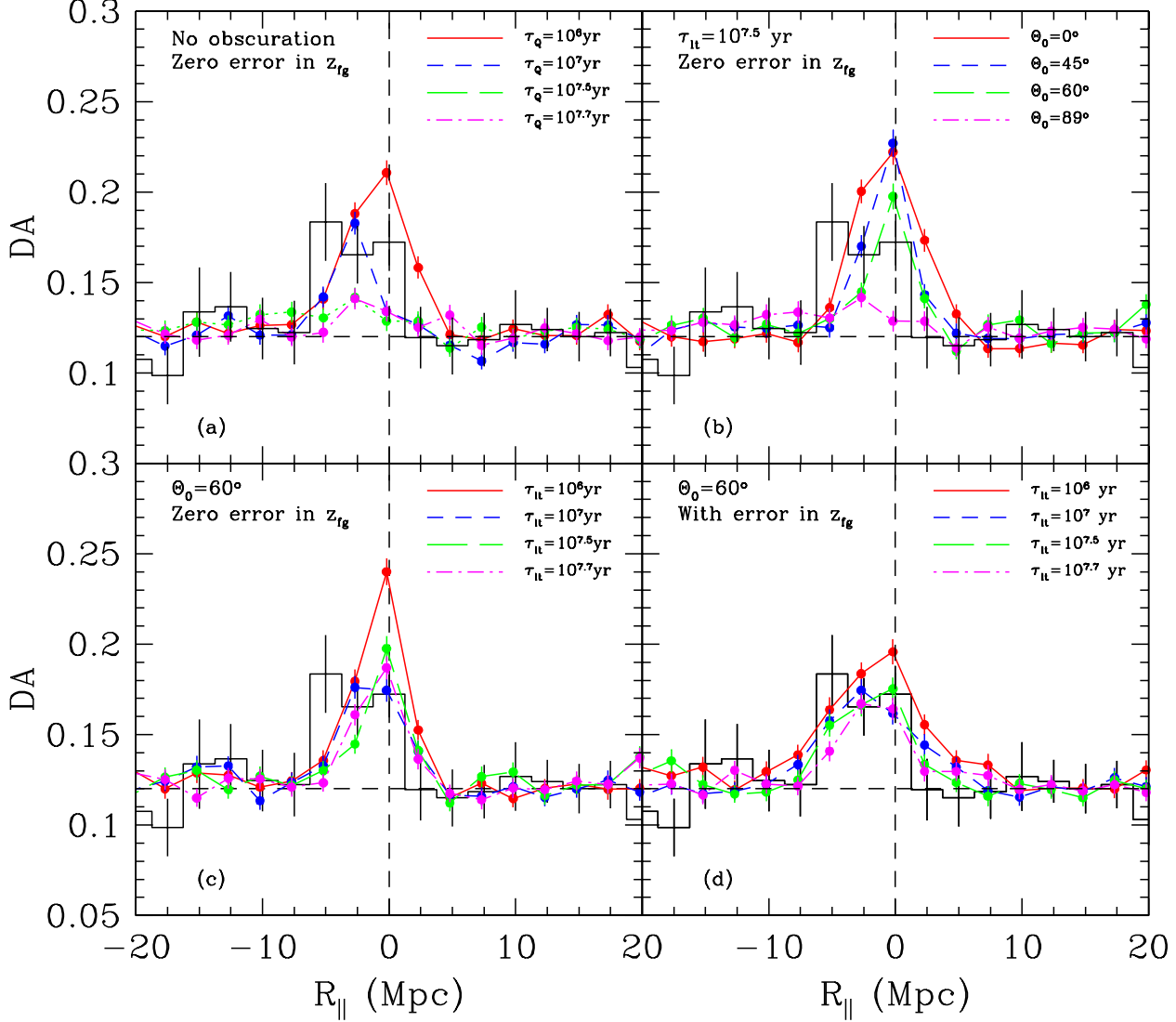


FIG. 3.— The transverse proximity effect for type 1 foreground QSOs at redshift ~ 2 . The histogram shown in each panel represents the average flux decrement DA obtained by KT08 for a sample of background QSOs as a function of proper distances along the sightline, with the origin corresponding to the redshift of the paired fgQSOs; and other lines and symbols represent our simulation results. In panel (a), the simulation results of DA is obtained under the assumption that there is no obscuration to the fgQSO UV radiation and no error in the estimates of the systemic redshifts of fgQSOs. Different colors represent different QSO ages, as labeled in the panel. Panel (b) shows the simulation results obtained by assuming that the QSO lifetime is $10^{7.5}$ yr, and the QSO age is randomly chosen over a range from 0 to each assumed QSO lifetime. Different colors represent different half-opening angles of the torus associated with each fgQSO Θ_0 . Panel (c) shows the simulation results obtained with $\Theta_0 = 60^\circ$ and different values of QSO lifetime. All the simulations in panels (a)–(c) assume a zero error in the estimates of the fgQSO systemic redshift. Panel (d) shows the simulated DA obtained by the same assumptions as those in panel (c), except for accounting for both the systematic and random errors in the estimates of the fgQSO systemic redshift. All the circle points shown in the figure are centered on the same bins of $R_{||}$ as the observational data but have been slightly offset to the left for graphical clarity (similarly in Figures 5 and 6 below).

duced if the lifetime of fgQSOs is $\sim 10^{7.5}$ yr (green line and points). Our calculations also show that the expected DA for cases with $\tau_t \lesssim 10^6$ yr cannot match the observations for any given Θ_0 , which is different from the suggestion that the fgQSOs have had their current UV luminosities for less than approximately a million years made in KT08. Our results suggest that the lifetime of the fgQSOs is consistent with being a few times 10^7 yr and a substantially smaller lifetime ($\lesssim 10^6$ yr) is not required by the PE, and it is also consistent with those constraints obtained by the detections of the TPE through He II Ly α forest or metal absorption lines (e.g., Jakobsen et al. 2003; Worseck & Wisotzki 2006; Worseck et al. 2007; Gonçalves et al. 2008).

Note here that the two components of some QSO pairs in KT08 are at similar redshift and therefore the TPE of those fgQSOs may be affected by the bgQSOs. The UV light from the bgQSO near a fgQSO may contribute some to the ionization of the near zone of the fgQSO, but this effect should be more significant at the backside than the front side of the fgQSO and lead to a more significant decrease in the DA at $R_{||} \sim -3 - -5$ Mpc. This effect cannot explain the significant excess of DA at $R_{||} \sim -3 - -5$ Mpc but rather require a more significantly enhanced density in the fgQSO near zone. In addition, if the density is also enhanced in the near zone of the bgQSOs, a more significant excess of the absorption at $R_{||} \sim -5$ Mpc can be expected, which might bring

the observed DA at $R_{\parallel} = -5$ Mpc in better consistency and strengthen the above conclusions.

In order to check the significance of the sample variance on the TPE obtained by KT08, we again generate 100 realizations of mock samples, each with 130 synthetic Ly α spectra. Figure 4 shows the expected TPE for those mock samples with similar settings to that shown in Figure 3d. According to this Figure, the KT08 results are still consistent with that the QSO lifetime is as long as a few 10^7 yr and the torus half opening angle $\Theta_0 \sim 60^\circ$. For the cases of $\tau_t \lesssim 10^6$ yr, the probability that the inconsistency between the KT08 TPE results and the expected TPE are simply due to sample variance is low.

There are still some uncertainties in the current estimation of UVB which may affect the simulation results. In our calculations, we set the UVB as $\Gamma_{\text{UVB}} = 10^{-12}\text{s}^{-1}$, which might be somewhat large as the latest estimation of Faucher-Giguère et al. (2008a) is only $0.5 \times 10^{-12}\text{s}^{-1}$. If the UVB is set to be this smaller value, a more significant LOSPE would be expected, and the effective density enhancement factor $\langle\Delta(R)\rangle$ should be slightly larger compared to that in Section 4.1 in order to fit the LOSPE estimated by KT08. Therefore, the QSO lifetime τ_t and/or the torus opening angle Θ_0 are required to be even larger than that given in Section 4.1 in order to reproduce the TPE. But if the UVB is unreasonably much larger than 10^{-12}s^{-1} , the excess of absorption at the transverse direction detected by KT08 cannot be explained by simply changing τ_t , Θ_0 and $\langle\Delta(R)\rangle$.

We caution here that other uncertainties could also affect the results presented here quantitatively. First, the DA estimated from observations may be affected by the continuum fitting. However, the error in the continuum fitting is typically on the percentage level depending on the signal-to-noise ratio of the QSO spectrum (Kim et al. 2007), which is not likely to change the observational results by KT08 on PE qualitatively. Second, the combined sample in KT08 are obtained from several different instruments and is highly heterogeneous. The ignoring of the detailed exact redshift and luminosity distributions of the QSO pairs in our simulations is sufficient for the demonstration purpose in this paper, but it may introduce some uncertainties to the resulted PE. Future works on extracting QSO properties from the PEs should consider the uncertainties. In addition, the luminosity of QSOs may evolve or fluctuate on timescales 10^6 yr, which may lead to more significant excess of absorption in the transverse directions (Adelberger 2004). However, such a luminosity variation of QSOs is not required according to our simulations.

Figure 5 shows the expected DA obtained from the mock samples by assuming that both the systematic and random errors in the estimates of the fgQSO systemic redshifts through CIV are the same as those adopted in KT08. Compared to the density enhancement used in Figure 2, here a larger value of it is used so that the LOSPE of fgQSOs obtained by KT08 can also be reproduced well (see the red line and points in Figure 5a). With the density enhancement required by the LOSPE, the DA distribution near the fgQSOs indicated by the bgQSO spectra (i.e., the TPE) is also calculated as shown in Figure 5b. We find that the observational asymmetric distribution of the excess in DA near $R_{\parallel} \sim 0$, i.e., the lack of excess in DA at $R_{\parallel} \sim 2.5$ Mpc and the significant

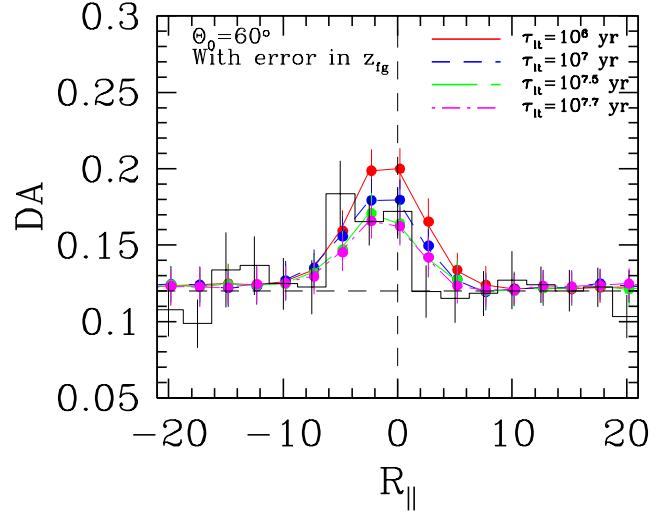


FIG. 4.— The transverse proximity effect of fgQSOs expected from 100 realizations of mock samples each with 130 synthetic Ly α forest spectra. Legends are similar to that for Figure 3d, except the errorbar to each bin is the standard deviation of the sample.

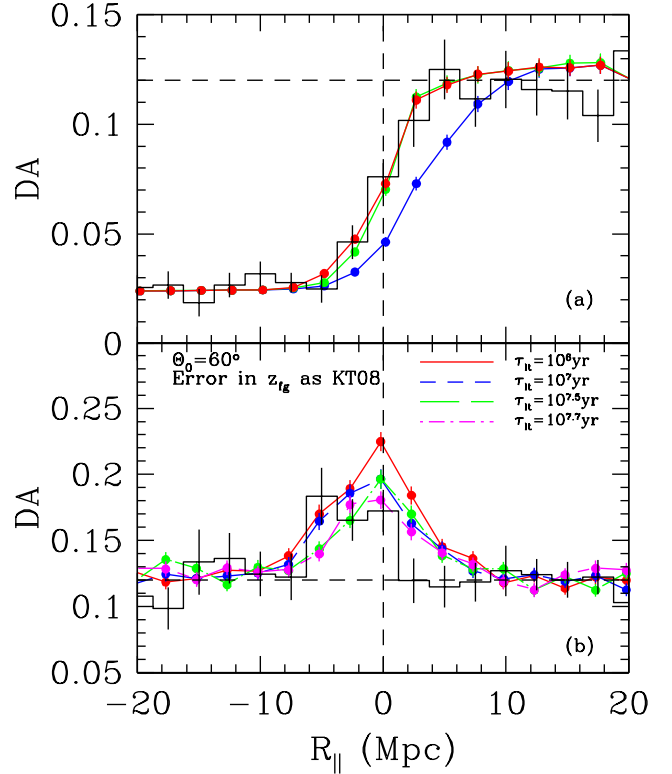


FIG. 5.— The line of sight proximity effect and the transverse proximity effect of fgQSOs that both the systematic and random errors in their systemic redshift estimation used are the same as that in KT08. Legends of panel (a) are similar to those of Figure 3 and legends of panel (b) are similar to those of Figure 3d.

excess of DA at $R_{\parallel} \sim -5$ Mpc, cannot be simultaneously re-produced for any given τ_t and Θ_0 , in contrast to the results in Figures 3d and 4.

4.1.3. The TPE of type 2 fgQSOs

Assuming that the effect of the density enhancement near type 2 fgQSOs is the same as that of type 1 fgQSOs with similar intrinsic L_{ν_0} constrained by the LOSPE (see Figure 2), we generate synthetic Ly α forest spectra

of type 1 bgQSOs whose light passed by the proximity region of type 2 fgQSOs to study the TPE of type 2 fgQSOs. Figure 6 shows our simulation results on their DA distribution near the fgQSOs. Figure 6a shows the dependence of the TPE on the half opening angle of the torus Θ_0 for the mock samples of type 2 fgQSOs, given the QSO lifetime. As seen from the panel, generally the larger the Θ_0 , the less the excess of the absorption near $R_{\parallel} \sim 0$ Mpc. Figure 6b shows the dependence of the TPE on the QSO lifetime, given the half opening angle $\Theta_0 = 60^\circ$. As seen from the panel, the differences in DA are relatively small among the cases with large τ_{lt} ($\sim 10^7 - 10^{7.7}$ yr). If $\tau_{lt} \sim 10^6$ yr, the absorption at $R_{\parallel} \sim 0$ Mpc is larger than those cases with large τ_{lt} due to the time-delay effect. Generally the absorption in the region closer to the observer ($R_{\parallel} > 0$) should be relatively large compared to that for type 1 fgQSOs (see Figure 3d), because the near side is more likely to be obscured from the fgQSOs. That effect, though weak, is shown in Figure 7 (see some relative deep dips of the curves at $R_{\parallel} \sim 2.5$ Mpc). This contrast between the absorption DA of type 2 fgQSOs and that of type 1 fgQSOs appears more significant for higher luminosity mock samples, as will be seen in Section 4.2.3 and Figure 11 below.

Note that in this paper, the UV radiation is assumed to be intrinsically isotropic, after removing the anisotropic effect due to the torus. However, if the UV radiation is intrinsically anisotropic, the TPE of type 2 fgQSOs may be different from those expected from the above calculations. For example, if the UV (and X-ray) radiation is relatively stronger along the direction of the torus axis than in the direction along the torus plane, the expected DA excess for type 2 fgQSOs should be smaller at $R_{\parallel} \sim 0$ Mpc than those calculated above.

4.2. High-luminosity samples at $z \sim 4$

4.2.1. The LOSPE of type 1 fgQSOs

Figure 8 shows the optical depth distribution near QSOs/fgQSOs along their LOSs with the origin corresponding to their redshift (similar to Figure 2). The red points with errorbars show the results obtained by Guimarães et al. (2007) for an observational sample of ~ 50 high-redshift QSOs ($z \sim 4$) with mean Lyman limit luminosity of $L_{\nu_0} \sim 8 \times 10^{31} \text{ erg s}^{-1} \text{ Hz}^{-1}$. The blue open circles represent the median optical depth obtained from our mock sample with 500 spectra affected by fgQSOs by assuming that the density distribution near the fgQSOs is the same as that of the cosmic average, which are clearly offset from the observations. Note that the errors in the estimates of the fgQSO systemic redshift are also considered in our simulation here by adopting the method same as that used in Guimarães et al. (2007), i.e., the error is randomly chosen over the range of $0 - 1500 \text{ km s}^{-1}$. The decrease of the simulated optical depth with decreasing distance to the QSOs appears more significant than the observation results, as the effect of the density enhancement in the proximity regions of these QSOs is ignored. Assuming that the density in the QSO proximity regions is enhanced by a factor of $\langle \Delta(R) \rangle \sim 1 + C_0(R/C_R)^{-p} \exp[-(R/C_R)^q]$, the observations can be reproduced by simulations (blue solid

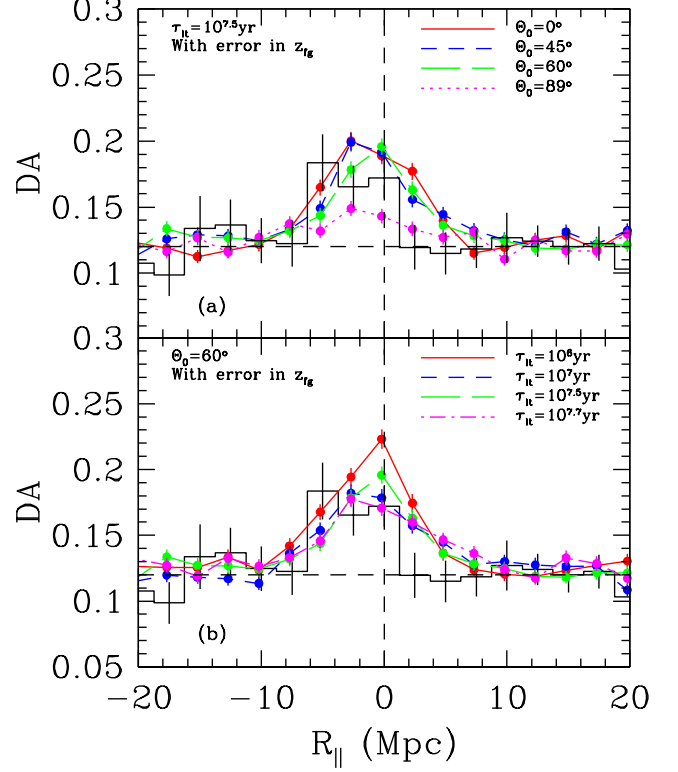


FIG. 6.— The transverse proximity effect for type 2 fgQSOs with the same intrinsic luminosity L_{ν_0} at redshift ~ 2 as those in Figure 3b and d. Legends for panel (a) and (b) are similar to those of Figure 3b and d, respectively. As a reference, the excess absorption near type 1 fgQSOs measured by KT08 is also shown by the histogram here.

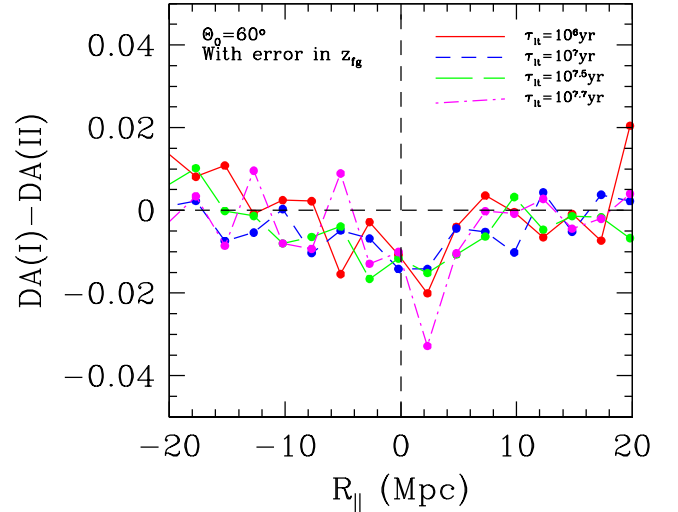


FIG. 7.— The difference of the transverse proximity effect between type 1 fgQSOs and type 2 fgQSOs shown in Figure 3d and Figure 6b. The flux decrement in the proximity region of type 1 fgQSOs and type 2 fgQSOs are represented by $DA(I)$ and $DA(II)$, respectively. Legends are similar to those in Figure 3d.

circles) if $C_0 = 0.9$, $C_R = 11$ Mpc, $p = 0.7$, and $q = 0.5$.³ For this case, we set the number of spectra in each realization to be 50 and we simulate 100 realizations. Thus

³ With the adopted parameters here, the effective density enhancement is almost the same as that required for the low-luminosity sample of KT08 at $R < 3$ Mpc but declines slower at $R > 3$ Mpc (see Section 4.1).

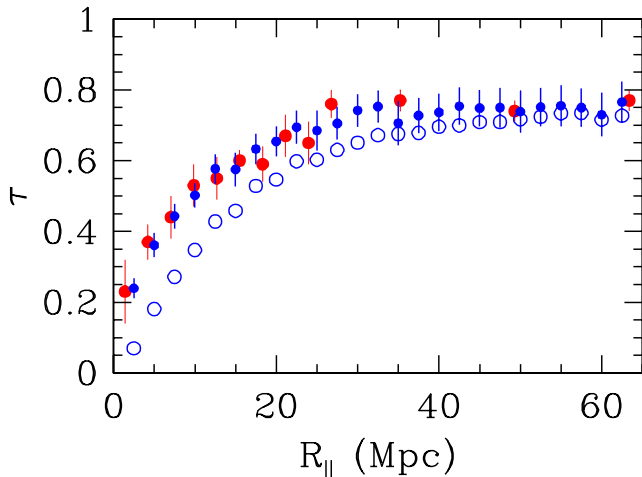


FIG. 8.— The line of sight proximity effect for type 1 QSOs. The red points show the optical depth distribution in the QSO proximity region obtained by Guimarães et al. (2007) for an observational sample of QSOs with a mean Lyman limit luminosity of $\sim 8 \times 10^{31} \text{ erg s}^{-1} \text{ Hz}^{-1}$ at redshift ~ 4 . The blue open circles represent the optical depth distribution obtained from our simulated mock sample by assuming that the density in the QSO proximity regions is the same as that of the cosmic average. The blue solid circles with errorbars represent the simulated results by assuming that the density distribution in the QSO proximity region is enhanced by a factor of $\Delta(R)$ (see details in Section 4.2.1).

the mean median optical depth and its standard deviation can be estimated from these realizations. As seen from Figure 8, the observations can be well matched by the simulation results (blue solid points).

Guimarães et al. (2007) also suggest that the density enhancement in the near zones of QSOs is required in order to explain their measurements on the LOSPE. Compared with their estimates on the density enhancement in the near zones of those high luminosity QSOs, our estimates are smaller by a factor of 1.5 – 5 at a distance of $R_{\parallel} \lesssim 10 \text{ Mpc}$ but similar at a distance of $R_{\parallel} \gtrsim 15 \text{ Mpc}$. The main reason for this difference is that the Poisson variance of absorption lines in different sight lines to the near zones of QSOs, which is included in the Monte-Carlo simulations here, leads to an averaged absorption that is larger than a simple estimation obtained without considering of the Poisson variance (see Guimarães et al. 2007). Therefore, the density enhancement required here is less significant compared with that obtained by Guimarães et al. (2007) (see also discussions on the Poisson variance in Dall’Aglio et al. 2008).

4.2.2. The TPE of type 1 fgQSOs

Although so far there is no observational measurement on the TPE of QSOs (with luminosity $\sim 8 \times 10^{31} \text{ erg s}^{-1} \text{ Hz}^{-1}$) similar to the sample in Guimarães et al. (2007), we illustrate here the effects of different QSO properties on the TPE and demonstrate that both τ_t and Θ_0 can be simultaneously constrained by the TPE if the density enhancement in the fgQSO proximity region has been constrained by the LOSPE. We first assume that the effect of the density enhancement in the proximity regions of those QSOs is the same as that indicated by the LOSPE obtained by Guimarães et al. (2007) (see Figure 8). Under this assumption, we synthesize a large number of Ly α forest spectra of bgQSOs with different choices of the QSO life-

time and the half opening angle of the associated torus (see parameter settings in Section 2). We then extract the median optical depth distribution in the fgQSO proximity regions from these spectra and show the results in Figure 9. As seen from Figure 9a, given the half opening angle of the torus associated with the fgQSO, e.g., $\Theta_0 = 60^\circ$, generally the optical depth in the proximity region to the QSO (e.g., $|R_{\parallel}| \lesssim 10 \text{ Mpc}$) decrease with increasing the QSO lifetime; and the decrease is significant initially at the frontside to the QSO, and becomes significant at its backside (e.g., $R_{\parallel} \sim -4 \text{ Mpc}$) when the QSO lifetime τ_t is long enough so that the region can be reached by the radiation from the fgQSO. That tendency is manifest especially for large Θ_0 , as (1) for the case with short QSO lifetime (e.g., $\tau_t \sim 10^{6.3} \text{ yr}$; see Figure 9b), the insignificant decrease of the optical depth is not sensitive to different choices of Θ_0 ; and (2) as shown in Figure 9c and d, for large τ_t , the decrease of the optical depth at $R_{\parallel} \lesssim 0 \text{ Mpc}$ increases with increasing large Θ_0 . As shown in the figure, the QSO lifetime and the half opening angle of the torus affect the optical depth curves in different ways, so that they can be simultaneously constrained by the LOSPE and TPE of QSOs if τ_t and Θ_0 are not too small (e.g., $\tau_t \gtrsim 10^6 \text{ yr}$ and $\Theta_0 \gtrsim 30^\circ$). Note here that the standard deviation, on the order similar to that shown in Figure 9, is small enough so that the constraints on the QSO lifetime and the torus half opening angle may be accurately extracted through the PEs of a sample with a few hundreds of high luminosity QSOs.

Considering the possibility of inaccuracy in the errors of the QSO systemic redshifts used above, we also test that our results obtained above remain the same qualitatively, if the systemic redshift errors is set to be the same as that for the low-luminosity low-redshift sample in Section 4.1.2. The overall shape of the optical depth distribution around $R_{\parallel} \sim 0 \text{ Mpc}$ does not change significantly, though it may shift slightly toward the negative R_{\parallel} direction, as discussed in Section 4.1.2.

4.2.3. The TPE of type 2 fgQSOs

Assuming that the effect of the density enhancement near type 2 fgQSOs is the same as that of type 1 fgQSOs with similar $L_{\nu_0} \sim 8 \times 10^{31} \text{ erg s}^{-1} \text{ Hz}^{-1}$ at $z \sim 4$, we show our simulated TPE of these type 2 fgQSOs in Figure 10. As seen from Figure 10a, given the half opening angle of the torus (e.g., $\Theta_0 = 60^\circ$), the larger the QSO lifetime τ_t , the smaller the optical depth at $R_{\parallel} \sim 0 \text{ Mpc}$ because the UV photons from the fgQSOs are more likely to propagate to more distance regions in the transverse direction. Given the QSO lifetime, the larger the half opening angle of the torus, the smaller the optical depth at $R_{\parallel} \gtrsim 0 \text{ Mpc}$ (Figure 10b).

Figure 11 shows the difference between the optical depth distribution near type 2 fgQSOs and that near type 1 fgQSOs, assuming that other parameters of these two types of fgQSOs (e.g., τ_t and Θ_0) are the same. In contrast to the cases considered for fgQSOs with $L_{\nu_0} \sim 5 \times 10^{30} \text{ erg s}^{-1} \text{ Hz}^{-1}$ at redshift ~ 2 , the difference here is obvious at the near side of the fgQSOs and for some cases in the far side because the fgQSOs in the mock samples here are much more luminous than that in Section 4.1.3. Given the half opening angle of the torus, $\Theta_0 = 60^\circ$, the optical depth difference at $R_{\parallel} \sim 0\text{--}15 \text{ Mpc}$

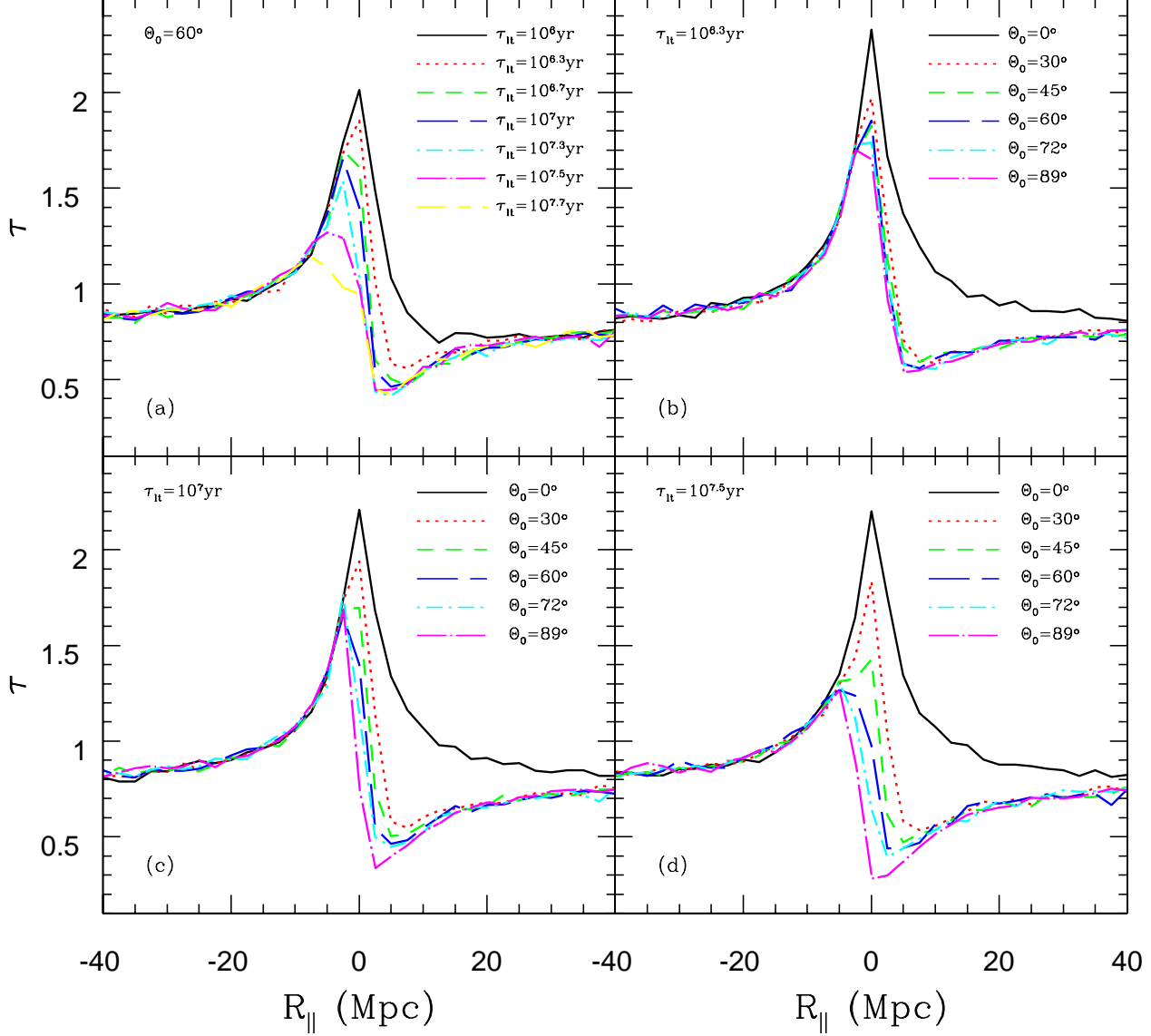


FIG. 9.— The expected transverse proximity effect of type 1 fgQSOs at redshift ~ 4 with Lyman limit luminosity of $L_{\nu_0} \sim 8 \times 10^{31} \text{ erg s}^{-1} \text{ Hz}^{-1}$. Panel (a) shows the expected optical depth distribution in the proximity region of fgQSOs, in which the half opening angle of each fgQSO is assumed to be 60° and different curves represent the results obtained for different sets of the fgQSO lifetime τ_t . The other three panels show the dependence of the optical depth on the half opening angle of the torus, given the fgQSO lifetime $\tau_t = 10^{6.3}, 10^7, 10^{7.5}$, respectively.

increases with increasing τ_t but saturates when $\tau_t \gtrsim$ a few times 10^7 yr; while the difference at the far side $R_{||} < 0$ only becomes visible when $\tau_t \gtrsim 10^7$ yr. Given a QSO lifetime, the optical depth difference is close to 0 for either small half opening angle of torus $\Theta_0 \rightarrow 0^\circ$ or large $\Theta_0 \rightarrow 90^\circ$; however, this difference is the largest for a medium $\Theta_0 \sim 60^\circ$. That behavior of the optical depth difference is the combined effects due to the geometrical nature of the torus and the time delay of photons that propagated to the backside of fgQSOs. The sharp contrast of the TPE due to type 1 fgQSOs from that due to type 2 fgQSOs should be useful to probe the properties of QSOs through the PE.

The simulated results illustrated above for the fgQSOs similar to that in the sample of Guimarães et al. (2007) again suggest that the QSO properties, such as the density enhancement in its proximity region, the lifetime and the opening angle of the associated torus, can be constrained simultaneously by the LOSPE and TPE

of type 1 (and/or type 2) fgQSOs. As the fgQSOs in these samples are much more luminous, their TPE is obvious, without being smeared out by the errors in the systemic redshift estimates of the fgQSOs.

5. CONCLUSIONS AND DISCUSSIONS

In this paper, we have investigated both the LOSPE and the TPE due to type 1 QSOs and the TPE due to type 2 QSOs. To do so, we adopted the Monte-Carlo method to generate a large number of simulated Ly α forest spectra of type 1 bgQSOs that may be affected by (fg)QSOs, according to the statistical distributions of the HI column density, the Doppler parameter of the Ly α absorption lines, and the number evolution of the absorbers associated with these absorption lines. We extracted the distribution of the flux decrement (DA) or the optical depth near the fgQSOs from these spectra. We illustrated that the effects of the fgQSOs on the bgQSO spectra depend on the fgQSO lifetime, the anisotropy in the

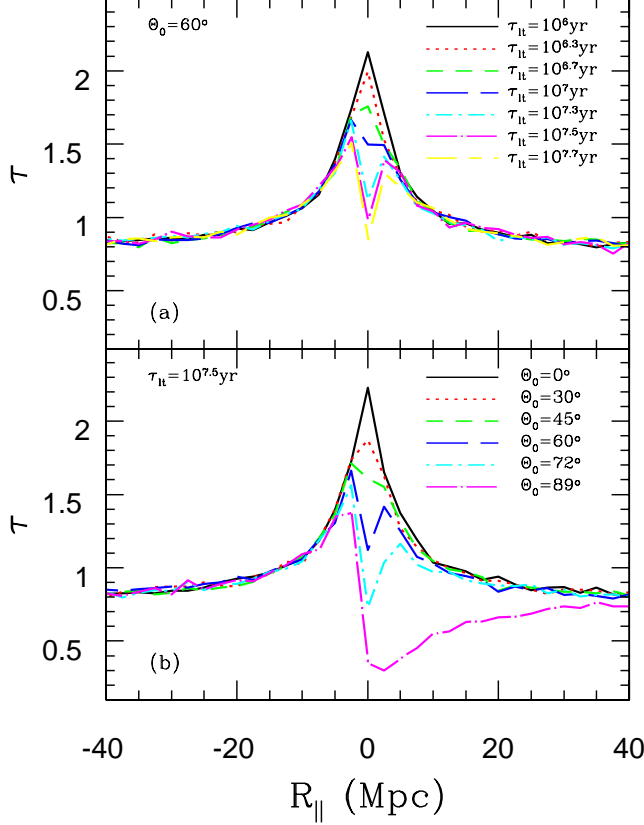


FIG. 10.— The expected transverse proximity effect of type 2 QSOs at redshift ~ 4 . Legends for panels (a) and (b) are the same as those for Figure 9a and d, respectively. See details in Section 4.2.3.

fgQSO UV radiation, and the density enhancement in the fgQSO proximity region, given the strength of the UVB. According to these calculations, the PE of QSOs may be divided into the ionization proximity effect (IPE) and the density proximity effect (DPE). The absorption near a QSO may be enhanced due to the DPE but decrease due to the IPE. Depending on detailed properties of QSOs, the combination of DPE and IPE can result in either an excess or a decrease of absorption in the near zone of a fgQSO.

The LOSPE of a QSO with known luminosity is affected by the density enhancement in the QSO near zone but irrelevant to the QSO lifetime and the anisotropy in the QSO UV radiation, which can thus provide constraint on the effective density enhancement in the near zone of the QSO. Based on the measurements of LOSPE for a low-redshift low-luminosity QSO sample (i.e., $z \sim 2$ and $L_{\nu_0} \sim 5 \times 10^{31} \text{ erg s}^{-1} \text{ Hz}^{-1}$; see KT08) or a high-redshift high luminosity QSO sample (i.e., $z \sim 4$ and $L_{\nu_0} \sim 8 \times 10^{31} \text{ erg s}^{-1} \text{ Hz}^{-1}$; see Guimarães et al. 2007), we obtained the effective density enhancement in the near zones of the QSOs in these two samples by matching the numerical results to the observations, respectively. Assuming that the density enhancement in the near zones of the fgQSOs is the same as that obtained from the LOSPE, the TPE has been simulated for both type 1 and type 2 fgQSOs with a wide range distribution of the fgQSO properties, i.e., the lifetime and the half opening angle of the associated tori. Our numerical simulations show that the response of the TPE to the change in the fgQSO lifetime (or the luminosity evolution or fluctua-

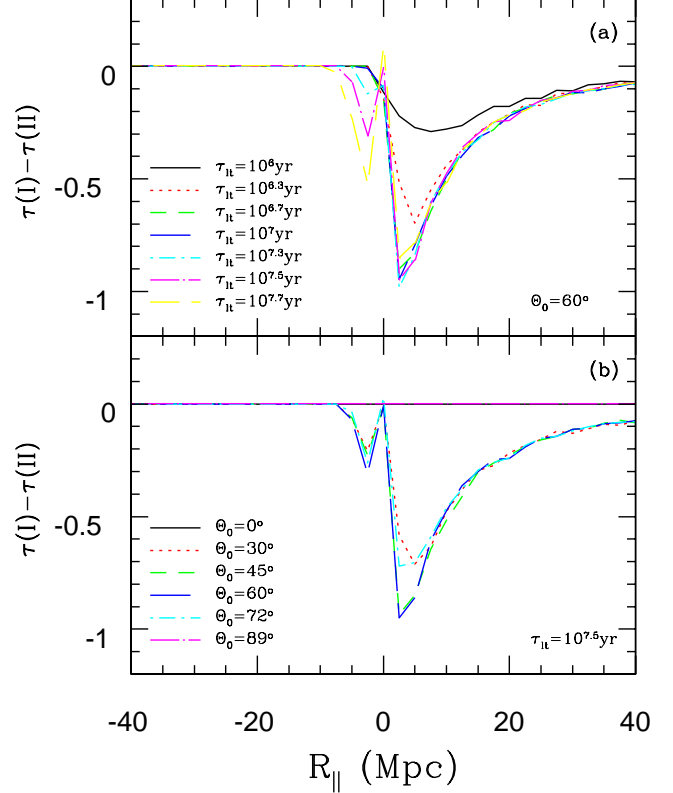


FIG. 11.— The expected difference in the transverse proximity effect of type 1 fgQSOs at redshift ~ 4 from that of type 2 fgQSOs. The optical depth distribution near type 1 fgQSOs is denoted by $\tau(\text{I})$, and that near type 2 fgQSOs denoted by $\tau(\text{II})$. Legends are the same as those for Figure 10. See details in Section 4.2.3.

tion on timescale of $10^6 - 10^7$ yr) and that to the change of the half opening angle of torus are different. The differences in the resulted TPE for different settings of the QSO lifetime are large for the high-luminosity samples, but they are relatively small for the low-luminosity sample. These results suggest that the density enhancement near the fgQSOs, the fgQSO lifetime and the half opening angle of the tori associated with the fgQSOs can be simultaneously constrained by the LOSPE and the TPE combined together of a sample with several hundreds bright QSOs. If a significant number of type 2 QSOs can be revealed by future observations, our simulations show that the TPE of type 2 QSOs can be significantly different from that of type 1 QSOs, and an observational search for the contrast will further help to distinguish the different effects due to QSO properties or environment and improve the constraints.

The lifetime and the opening angle of the torus are of fundamental importance for our understanding of the QSO physics and the growth of massive black holes (MBHs). The lifetime of QSOs is an important parameter characterizing the luminosity evolution of QSOs and thus the assembly history of MBHs (including the mass and the spin evolution). A number of independent arguments suggest that the lifetime of bright QSOs is on the order of $10^7 - 10^8$ yr (e.g., Haiman & Hui 2001; Martini & Weinberg 2001; Yu & Tremaine 2002; Steidel et al. 2002; Yu & Lu 2004; Marconi et al. 2004; Yu & Lu 2008; Shen 2009; Shankar et al. 2010; also see a review by Martini 2004). However, in principle, MBH growth may occur mainly through a long period contin-

uous accretion or alternatively many short-period accretion episodes; and those numbers are mainly obtained from demography of QSOs and they may only represent the net lifetime that the QSO luminosity in some wavelength range larger than a threshold, not the time period for each accretion episode (e.g., see Martini 2004). As we have demonstrated that the TPE offers a way, if not the only way, to constrain the episodic lifetime of QSOs (see also Adelberger 2004), which should provide considerable insight into our understanding of the growth history of MBHs. The presence of a torus surrounding each QSO is proposed to be the underlying reason that leads to the classification of type 1 QSOs and type 2 QSOs. The half opening angle of the torus is an important parameter that determines the ratio of type 2 to type 1 QSOs. As demonstrated in this paper, the TPE, together with the LOSPE, can provide constraints on this angle, which is independent of those previous ways mainly through observational ratios of type 2 to type 1 QSOs (e.g., Treister & Urry 2006; Gilli et al. 2007; Treister et al. 2010). As an alternative potential tool to constrain the opening angle of the torus, the QSO PE may be helpful in our understanding of the unification picture of different types of the AGN population and its underlying physics.

KT08 measured both the LOSPE and the TPE for a low-redshift low-luminosity QSO sample ($z \sim 2$ and $L_{\nu_0} \sim 5 \times 10^{30} \text{ erg s}^{-1} \text{ Hz}^{-1}$), and their measurement on the TPE suggested that the QSO lifetime is $\lesssim 10^6$ yr. That is apparently in contradiction with the detections of the TPE through other observations on He II or metal lines, which require a longer QSO lifetime $\tau_Q \gtrsim (2 - 3) \times 10^7$ yr (e.g., Jakobsen et al. 2003; Worseck & Wisotzki 2006; Worseck et al. 2007; Gonçalves et al. 2008). Through our Monte-Carlo simulations, we have shown that the apparent contradiction can be solved after considering a combination of the effects due to density enhancement in the near zone of the fgQSOs and the obscuration of the tori associated with the fgQSOs.

Guimarães et al. (2007) measured the LOSPE for a high-redshift high-luminosity sample ($z \sim 4$ and $L_{\nu_0} \sim$

$8 \times 10^{31} \text{ erg s}^{-1} \text{ Hz}^{-1}$), and their LOSPE measurement suggests that the density in the near zones of those QSOs is enhanced. In order to reproduce their measurement on the LOSPE, a density enhancement is also required in our Monte-Carlo simulations. Compared with Guimarães et al. (2007) estimates on the density enhancement, the required density enhancement here is smaller by a factor of $1.5 - 5$ at a distance of $R_{\parallel} \lesssim 10 \text{ Mpc}$ but similar at a distance of $R_{\parallel} \gtrsim 15 \text{ Mpc}$. The main reason for this difference is that the Poisson variance of absorption lines in the near zones of QSOs, which is included in our Monte-Carlo simulations, leads to an averaged absorption that is larger than a simple estimation obtained without considering of the Poisson variance (see Guimarães et al. 2007). Therefore, a less significant density enhancement is required here compared with that obtained by Guimarães et al. (2007) (see also discussions on the Poisson variance in Dall’Aglio et al. 2008).

We conclude that the current measurements on the LOSPE and the TPE are consistent with that (1) the density is significantly enhanced in the vicinity of fgQSOs, (2) the fgQSO lifetime is longer than a few 10^7 yr and a much shorter lifetime (i.e., $\lesssim 10^6$ yr) is excluded or at least is not required, and (3) the half opening angle of the tori associated with fgQSOs is $\sim 60^\circ$, which are consistent with other independent estimates (e.g., Jakobsen et al. 2003; Worseck & Wisotzki 2006; Worseck et al. 2007; Gonçalves et al. 2008; Treister & Urry 2006; Gilli et al. 2007; Treister et al. 2010). Future observations on the PE of several hundreds of bright type 1 and type 2 (fg)QSOs will potentially set accurate constraints simultaneously on these QSO properties.

ACKNOWLEDGMENTS

This work was supported in part by the National Natural Science Foundation of China under No. 10973001, 10973017, 11033001, and the Bairen program from the National Astronomical Observatories, Chinese Academy of Sciences.

APPENDIX

INTERSECTIONS OF THE LIGHT CONE CONFINED BY THE TORUS AND THE SURFACE CONFINED BY THE TIME-DELAY EFFECT

The light cone confined by the dusty torus associated with the central engine of a QSO is given by

$$\begin{aligned} X^2 + (Y \cos \Psi_0 - R_{\parallel} \sin \Psi_0)^2 \\ - (Y \sin \Psi_0 + R_{\parallel} \cos \Psi_0)^2 \tan^2 \Theta_0 = 0, \end{aligned} \quad (\text{A1})$$

where (X, Y, R_{\parallel}) are the three-dimensional Cartesian coordinates with the QSO being the origin, Θ_0 is the half opening angle of the torus, Ψ_0 is the offset of the torus axis from the LOS of the fgQSO (see Figure 1). The cylinder with a radius of R_{\perp} is defined as

$$X^2 + Y^2 = R_{\perp}^2, \quad (\text{A2})$$

where $X = R_{\perp} \sin \Phi$, $Y = R_{\perp} \cos \Phi$, and $\Phi \in [0^\circ, 360^\circ)$ is the rotation angle around the LOS. Figure 1 shows the cases for $\Phi = 0^\circ$. For any given Φ , the intersections of the light cone with the cylinder are the solutions of equations A1 and A2. If $\Phi = 0^\circ$, the two solutions are $R_{\parallel, \text{E}} = -R_{\perp} / \tan(\Theta_0 - \Psi_0)$ and $R_{\parallel, \text{F}} = R_{\perp} / \tan(\Theta_0 + \Psi_0)$ for type 1 QSOs (the left panel in Figure 1) or $R_{\parallel, \text{E}} = R_{\perp} / \tan(\Theta_0 + \Psi_0)$ and $R_{\parallel, \text{F}} = -R_{\perp} / \tan(\Theta_0 - \Psi_0)$ for type 2 QSOs (the right panel in Figure 1), respectively. For the case of $\Phi = 90^\circ$, the two solutions are $R_{\parallel, \text{E}} = -R_{\perp} / (|\cos \Psi_0| \sqrt{\tan^2 \Theta_0 - \tan^2 \Psi_0})$ and $R_{\parallel, \text{F}} = -R_{\parallel, \text{E}}$ if $|\tan \Theta_0| > |\tan \Psi_0|$; and there is no solution to the above two equations, otherwise. For those

cases without solutions to the above two equations, there is no the PE on the bgQSO spectrum due to the dusty torus associated with the type 2 fgQSO.

REFERENCES

- Adelberger, K. L. 2004, *ApJ*, 612, 706
 Bajtlik, S., Duncan, R. C., & Ostriker, J. P. 1988, *ApJ*, 327, 570
 Bolton, J. S., Haehnelt, M. G., Viel, M., & Springel, V. 2005, *MNRAS*, 357, 1178
 Carswell, R. F., Webb, J. K., Baldwin, J. A., & Atwood, B. 1987, *ApJ*, 319, 709
 Croft, R. A. C. 2004, *ApJ*, 610, 642
 Crofts, A. P. S., & Fang, Y. 1998, *ApJ*, 502, 16
 Dall’Aglio, A., Wisotzki, L., & Worsack, G. 2008, *A&A*, 491, 465
 Dall’Aglio, A., Wisotzki, L., & Worsack, G. 2009, arXiv:0906.1484
 Fernaández-Soto, A., Barcons, X., Carballo, R., & Webb, J. K. 1995, *MNRAS*, 277, 235
 Faucher-Giguère, C.-A., Lidz, A., Hernquist, L., & Zaldarriaga, M. 2008a, *ApJ*, 688, 85
 Faucher-Giguère, C.-A., Lidz, A., Zaldarriaga, M., & Hernquist, L. 2008b, *ApJ*, 673, 39
 Faucher-Giguère, C.-A., Prochaska, J. X., Lidz, A., Hernquist, L., & Zaldarriaga, M. 2008c, *ApJ*, 681, 831
 Gilli, R., Comastri, A., Hasinger, G. 2007, *A&A*, 463, 79
 Gonçalves, T. S., Steidel, C. C., Pettini, M. 2008, *ApJ*, 676, 816
 Guimarães, R., Petitjean, P., Rollinde, E., de Carvalho, R. R., Djorgovski, S. G., Srianand, R., Aghaee, A., & Castro, S. 2007, *MNRAS*, 377, 657
 Haiman, Z., & Hui, L. 2001, *ApJ*, 547, 27
 Haardt, F., & Madau, P. 1996, *ApJ*, 461, 20
 Hui, L., & Gnedin, N. Y. 1997, *MNRAS*, 292, 27
 Jakobsen, P., Jansen, R. A., Wagner, S., & Reimers, D. 2003, *A&A*, 397, 891
 Kim, T. S., Cristiani, S., & D’Odorico, S. 2001, *A&A*, 373, 757
 Kim, T.-S., Bolton, J. S., Viel, M., Haehnelt, M. G., & Carswell, R. F. 2007, *MNRAS*, 382, 1657
 Kim, Y.-R., & Croft, R. A. C. 2008, *MNRAS*, 387, 377
 Kirkman, D., & Tytler, D. 2008, *MNRAS*, 391, 1457
 Kirkman, D., et al. 2005, *MNRAS*, 360, 1373
 Komatsu, E., et al. 2009, *ApJS*, 180, 330
 Marconi, A., Risaliti, G., Gilli, R., Hunt, L. K., Maiolino, R., & Salvati, M. 2004, *MNRAS*, 351, 169
 Martini, P. 2004, in *Coevolution of Black Holes and Galaxies*, ed. L. C. Ho (Cambridge: Cambridge Univ. Press), 169
 Martini, P., & Schneider, D. P. 2003, *ApJ*, 597, L109
 Martini, P., & Weinberg, D. H. 2001, *ApJ*, 547, 12
 McDonald, P., & Miralda-Escudé, J. 2001, *ApJ*, 549, L11
 Meiksin, A., & White, M. 2004, *MNRAS*, 350, 1107
 Nestor, D., Hamann, F., & Hidalgo, P. R. 2008, *MNRAS*, 386, 2055
 Osterbrock, D. E. 1989, *Astrophysics of Gaseous Nebulae and Active Galactic Nuclei*. (Mill Valley, CA: Univ. Science Books), 14
 Rauch, M., et al. 1997, *ApJ*, 489, 7
 Richards, G. T., Vandenberg, D. E., Reichard, T. A., Hall, P. S., Schneider, D. P., Subbarao, M., Thakar, A. R., & York, D. G. 2002, *AJ*, 124, 1
 Rollinde, E., Srianand, R., Theuns, T., Petitjean, P., & Chand, H. 2005, *MNRAS*, 361, 1015
 Schaye, J. 2001 *ApJ*, 559, 507
 Schaye, J., et al. 2003, *ApJ*, 596, 768
 Schirber, M., Miralda-Escudé, J., & McDonald, P. 2004, *ApJ*, 610, 105
 Scott, J., Bechtold, J., Dobrzycki, A., & Kulkarni, V. P. 2000, *ApJS*, 130, 67
 Shankar, F., Crocce, M., Miralda-Escudé, J., Fosalba, P., & Weinberg, D. H. 2010, *ApJ*, 690, 20
 Shen, Y. 2009, *ApJ*, 704, 89
 Steidel, C. C., Hunt, M. P., Shapley, A. E., Adelberger, K. L., Pettini, M., Dickinson, M., & Giavalisco, M. 2002, *ApJ*, 576, 653
 Treister, E., Natarajan, P., Sanders, D.B., Urry, C. M., Schawinski, K., & Kartaltepe, J. 2010, *Science*, 328, 600
 Treister, E., & Urry, C. M. 2006, *ApJ*, 652, L79
 Tytler, D., et al. 2004, *ApJ*, 617, 1
 Urry, C. M., & Padovani, P. 1995, *PASP*, 107, 803
 Worsack, G., & Wisotzki, L. 2006, *A&A*, 450, 495
 Worsack, G., Fechner, C., Wisotzki, L., & Dall’Aglio, A. 2007, *A&A*, 473, 805
 Yu, Q., & Lu, Y. 2004, *ApJ*, 602, 603
 Yu, Q., & Lu, Y. 2008, *ApJ*, 689, 732
 Yu, Q., & Tremaine, S. 2002, *MNRAS*, 335, 965